Showcasing research from Dr Jingwei Hou and
Prof. Vicki Chen from the School of Chemical Engineering,
University of Queensland, Australia and Dr Thomas D. Bennett
from the Department of Materials Science and Metallurgy,
University of Cambridge, UK.

Interfacial engineering of a polymer–MOF composite by
in situ vitrification

Do you like toasting marshmallows over a campfire?
If so, please check how we borrow this concept to "toast"
our MOF composite materials. *In situ* vitrification of MOF
within polymeric matrix can effectively form new bonds
and reduce interfacial defects.

As featured in:

See Jingwei Hou *et al.*,
Chem. Commun., 2020, **56**, 3609.

ROYAL SOCIETY
OF **CHEMISTRY**

rsc.li/chemcomm

Check for updates

Interfacial engineering of a polymer–MOF composite by *in situ* vitrification†

Rijia Lin, [a] Jingwei Hou, [*a] Mengran Li, [a] Zhanke Wang, [a] Lei Ge, [b] Shichun Li, [c] Simon Smart, [ad] Zhonghua Zhu, [a] Thomas D. Bennett [e] and Vicki Chen [a]

Non-stoichoimetric crystalline ZIF-62 was used as the filler for a 6FDA-DAM polyimide-based composite membrane. *In situ* melting and vitrification of ZIF-62 was then performed, to yield the ZIF-62 glass phase (a_gZIF-62), within the polymer matrix. Focus ion beam scanning electron microscopy (FIB-SEM), thermal characterisation and membrane separation tests demonstrate the filling of voids at the MOF/polymer interface from the liquid phase of ZIF-62.

The chemical and structural versatility of metal–organic frameworks (MOFs) has led to a host of different applications including toxic gas capture, water harvesting, molecular sieving, drug delivery and catalysis.[1–3] Interest in MOFs is gradually shifting from new material development, which currently stands at over 70 000 structures,[4] to material assembly towards macroscopic structures. However, most MOF materials are synthesised as discrete polycrystalline powders, which render them difficult to process. Therefore, the knowledge gap between material synthesis and their practical application is still significant. Innovative techniques to circumvent the relatively 'soft' mechanical properties of MOFs including sol–gel processing have been proposed, but are typically limited to case-by-case bases.[4,5]

A more straightforward and scalable approach is the use of MOF–fillers in polymeric binders to impart mechanical strength and processability to MOF-based materials. A wealth of reports exist on the technique, with potential applications of the resultant MOF–polymer composites in adsorption columns, sensors, batteries and, particularly, mixed matrix membranes.[6] Optimal performance of

such materials however relies upon obtaining a solution to the typically poor compatibility between MOF and polymer phases.[7] For example, poor interfacial adhesion can generate nonselective defects, which are detrimental to the separation efficiency of membranes.[8] Several techniques have been implemented to mitigate this issue including pre-functionalization of the MOF surface,[9] *in situ* nucleation of MOF fillers within polymer matrices,[10] *in situ* polymerisation with the presence of MOF fillers,[11] morphological modification of MOF fillers,[12–14] and the use of interface agents.[15,16] A one step post-treatment involving thermal treatment would be particularly appealing, given the relative simplicity and industrial applicability. Progress has also been made here, though is limited to a few reports on the *in situ* formation of coordination bonds between polymeric substrates and MOF fillers *via* annealing.[17]

Recently, the overwhelming dominance of the crystalline state in the MOF field has begun to be challenged through the synthesis and application of non-crystalline, or amorphous MOFs in proton conduction, electrochemical applications, membrane separation and encapsulation.[17–19] The liquid MOF phase, alongside the glasses formed upon quenching are of particular interest.[20] The zeolitic imidazolate framework (ZIF) family have been extensively investigated, with melting demonstrated to proceed *via* breaking of metal–ligand coordinative bonds, without change in the stoichiometry. Subsequent quenching allows the disordered node-linker arrangement to be kinetically preserved by avoiding re-crystallisation. The resultant glass is, like the crystalline phase, composed of tetrahedral MN_4 nodes, although it has lost the long-range order of the crystalline materials. Liquid and glass MOFs enable numerous possibility in the fabrication of new MOF materials, such as MOF glass blend, flux melted MOF, MOF crystal-glass composite and functionalized MOF glasses.[21] Recent work on the reactive nature of several high temperature liquid ZIFs[22] together with the innate ability of glass to yield bulk properties not available in crystalline materials, *e.g.* the absence of grain boundaries and high processability.[23] The ZIF glass enables its shaping towards macroscopic structures at the molten liquid state. This drives us to use the liquid ZIF state to regulate the surface and interface properties of MOF-polymer composites (Fig. 1).

Non-stoichiometric ZIF-62 [$Zn(Im)_{1.95}(bIm)_{0.05}$],[24] referred to as ZIF-62-bIm$_{0.05}$ hereafter, was selected due to the low melting

[a] *School of Chemical Engineering, The University of Queensland, Brisbane 4072, Australia. E-mail: jingwei.hou@uq.edu.au*

[b] *Centre for Future Materials, University of Southern Queensland, Queensland 4300, Australia*

[c] *Institute of Chemical Materials, China Academy of Engineering Physics, Mianyang 621900, P. R. China*

[d] *Dow Centre for Sustainable Engineering Innovation, The University of Queensland, QLD 4072, Australia*

[e] *Department of Materials Science and Metallurgy, University of Cambridge, Cambridge, CB3 0FS, UK*

† Electronic supplementary information (ESI) available: Full experimental procedures for MOFs and composites synthesis, results of ^{1}H NMR, TGA, DSC, SEM, adsorption, XRD and FIB. See DOI: 10.1039/d0cc00664e
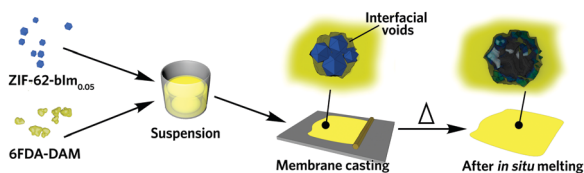
Fig. 1   Scheme of the preparation of glass ZIF-based mixed-matrix membranes.

temperature (T_m = 357.8 °C in Ar, Fig. S1, ESI†), and relatively high porosity in the glass state. The molar ratio of bIm/Im linker in ZIF-62 crystal and ZIF-62 glass is confirmed by liquid NMR (Fig. S2–S4, ESI†). Bulk octahedral crystals of ZIF-62-bIm$_{0.05}$ (*ca.* 100 μm) were first obtained from a hydrothermal synthesis in *N*,*N*-dimethylformamide (DMF) at 130 °C for 7 d, then the size of ZIF-62-bIm$_{0.05}$ was reduced by using a ball mill 1 h at a rotational speed of 800 rpm (*ca.* 1 μm, Fig. S5, ESI†). Extensive grinding was avoided to mitigate mechanical induced amorphisation (Fig. 2). The vitrification of this sample was confirmed according to the XRD results (Fig. 2a). After vitrification, the melt-quenched glass (termed as a$_g$ZIF-62-bIm$_{0.05}$ in line with our previous publications) shows a diffuse scattering centred at *ca.* 16°, indicating the collapse of the crystalline structure and the formation of the a$_g$ZIF-62-bIm$_{0.05}$ after vitrification. Scanning electron microscopic images confirmed the formation of coherent morphologies upon melt quenching (Fig. S5, ESI†).

The microporous structure of ZIF-62-bIm$_{0.05}$ before, and after melt-quenching was probed using CO_2 and N_2 adsorption isotherms (Fig. S6, ESI†). The surface area and pore size distribution of ZIF-62-bIm$_{0.05}$ and a$_g$ZIF-62-bIm$_{0.05}$ were fitted with a nonlocal density functional theory model (NLDFT, CO_2, 273 K, carbon with slit-pore geometry),[24,25] using experimental CO_2 adsorption isotherms collected at 273 K. The as-synthesized ZIF-62-bIm$_{0.05}$ crystal has a surface area (NLDFT) around 476 m² g⁻¹. a$_g$ZIF-62-bIm$_{0.05}$ still retains significant microporosity, with the surface area (NLDFT) being *ca.* 173 m² g⁻¹. This reduced surface area is mainly attributed

Fig. 2   (a) XRD spectra of ZIF-62-bIm$_{0.05}$ crystals and a$_g$ZIF-62-bIm$_{0.05}$ glass, (b) heat of CO_2 adsorption for ZIF-62-bIm$_{0.05}$ and a$_g$ZIF-62-bIm$_{0.05}$, (c) IAST adsorption selectivity of ZIF-62-bIm$_{0.05}$ crystal and a$_g$ZIF-62-bIm$_{0.05}$ for 50/50 CO_2/N_2 mixture at 303 K. (d) thermogravimetric (TG) and differential scanning calorimetry (DSC) analysis for (ZIF-62)$_{0.2}$(6FDA-DAM)$_{0.8}$ composite.

to the cavities loss at 3.2–5.3 Å due to the partial collapse of the framework, whilst the larger cavities at 5.3–6.3 Å are relatively better maintained (Fig. S6c, ESI†) and new cavities are formed at 6.3–7.3 Å.

At 303 K and 100 kPa, the gas uptakes for ZIF-62-bIm$_{0.05}$ are 40.1 cm³ g⁻¹ (CO_2) and 3.46 cm³ g⁻¹ (N_2) at 100 kPa, which reduces to 9.9 cm³ g⁻¹ (CO_2) and 0.16 cm³ g⁻¹ (N_2) for a$_g$ZIF-62-bIm$_{0.05}$. At the same time, a$_g$ZIF-62-bIm$_{0.05}$ exhibits a higher heat of adsorption for CO_2, compared to ZIF-62-bIm$_{0.05}$, which could be due to the presence of unsaturated metal sites rendering higher affinity to polar CO_2 gas molecules, or the reduced pore size rendering stronger host–guest interaction (Fig. 2b).[26] This leads to a significantly improved selectivity for 50/50 CO_2/N_2 binary mixture at 303 K, as calculated with ideal adsorbed solution theory (IAST) (Fig. 2c).

Polyimide 6FDA-DAM [6FDA = 2,2-bis(3,4-carboxyphenyl)-hexafluoropropanedianhydride, DAM = 2,4,6-trimethyl-*m*-phenyl-enediamine] was selected as the matrix for MOF composite fabrication, due to a high thermal stability (decomposition temperature, T_d > 450 °C, Fig. S7, ESI†), which lies above the ZIF-62 T_m.[27] Different weight percentages of the ZIF-62-bIm$_{0.05}$ filler were dispersed into the 6FDA-DAM chloroform solution (details are shown in the ESI†), then the solution was cast into a thin film for further study. The resultant composites were termed as (ZIF-62)$_x$(6FDA-DAM)$_{1-x}$ where x is the weight ratio of the ZIF.

The thin film morphology not only facilitates rapid and even heat transfer during the thermal treatment process, it also enables the examination of the composite film behaviour as molecular separation membranes. Upon heating at 20 °C min⁻¹ in Ar (Fig. 2d), the gradual loss of residual solvent occurs, until a major weight loss even begins at *ca.* 450 °C, attributed to the thermal decomposition of the polymeric matrix (Fig. S7, ESI†). The endothermic peak ending at *ca.* 390 °C suggests the *in situ* melting of ZIF-62-bIm$_{0.05}$, and the resultant composite is amorphous (Fig. S8, ESI†). It should be noted the T_m of ZIF-62-bIm$_{0.05}$ in composite is slightly higher than the pure crystal, attributed to a higher thermal transfer resistance of the polymer. Therefore, all the subsequent composite samples were treated at 390 °C in Ar to achieve complete melting of crystal ZIF-62 filler, and the composites after thermal treatment are termed as (a$_g$ZIF-62)$_x$(6FDA-DAM)$_{1-x}$.

The cross-sectional morphology of the composite films was examined with scanning electron microscopy (SEM), after being fractured in liquid nitrogen (Fig. S9, ESI†). For the (ZIF-62)$_{0.2}$(6FDA-DAM)$_{0.8}$, interfacial defects are observed for the fractured sample. These become more evident with higher filler loading due to aggregation of the ZIF-62 filler. After thermal treatment however, the interfaces between the a$_g$ZIF-62 and polyimide phases are much smoother. To further achieve more comprehensive structural information, the spatial distribution of fillers, voids and matrices for (ZIF-62)$_{0.2}$(6FDA-DAM)$_{0.8}$ and (a$_g$ZIF-62)$_{0.2}$(6FDA-DAM)$_{0.8}$ were examined by focused ion beam SEM (FIB-SEM, Fig. 3). The segmentation of the individual phases (filler, void and polymer phase) was conducted *via* image thresholding.[28,29] More information can be found in the ESI† (Fig. S10, S11 and Table S1, ESI†). For the (ZIF-62)$_{0.2}$(6FDA-DAM)$_{0.8}$, the presence of pinholes can be observed at the MOF/polymer interface, and within MOF aggregates, as suggested by the cross-sectional 2D image obtained under back-scattered electron mode (Fig. 3a). After *in situ* melting, a significant reduction in number and
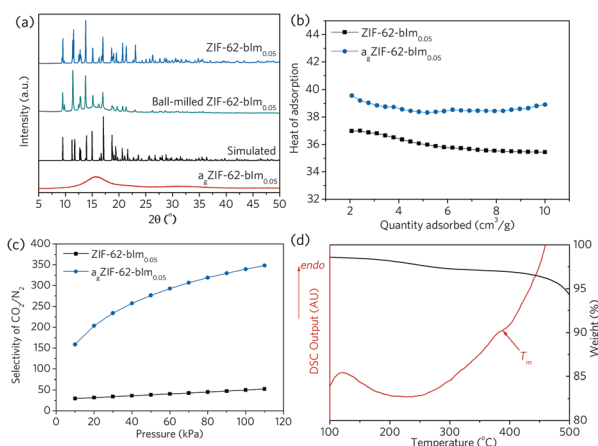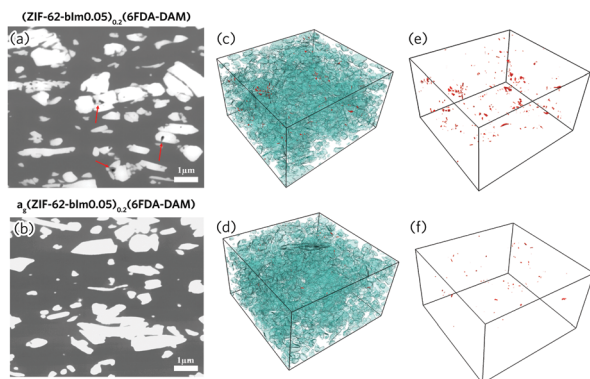
Fig. 3 FIB-SEM images and 3D reconstruction of MOF composite before (top) and after (bottom) thermal treatment. (a and b) 2D SEM images captured under BSE imaging mode with contrast difference of polymer matrix (grey), filler (white), and interfacial voids (black). (c and d) Surface-rendered view of the segmented FIB-SEM tomograms for $(ZIF-62)_{0.2}(6FDA-DAM)_{0.8}$ (c: fillers and voids; e: voids only) and $(a_gZIF-62)_{0.2}(6FDA-DAM)_{0.8}$ (d: fillers and voids; f: voids only). Box size of (c and e): 15.6 μm × 9.3 μm × 15.5 μm. Box size of $(a_gZIF-62)_{0.2}(6FDA-DAM)_{0.8}$ (d and f): 14.3 μm × 9.2 μm × 15.5 μm. 2D images captured under back-scattered electron (BSE) imaging mode with contrast difference of polymer matrix, filler, and interfacial voids, (a): $(ZIF-62)_{0.2}(6FDA-DAM)$; (b): $(a_gZIF-62)_{0.2}(6FDA-DAM)$. Surface-rendered view of the segmented FIB-SEM tomograms for $(ZIF-62)_{0.2}(6FDA-DAM)$ (c: fillers and voids; e: voids only) and $(a_gZIF-62)_{0.2}(6FDA-DAM)$ (d: fillers and voids; f: voids only). Box size of $(ZIF-62)_{0.2}(6FDA-DAM)$ (c and e): 15.6 μm × 9.3 μm × 15.5 μm. Box size of $(a_gzIF-62)_{0.2}(6FDA-DAM)$ (d and f): 14.3 μm.

size of pinholes is observed (Fig. 3a and b). This is further confirmed by 3D surface-rendered views of the MOF fillers (cyan) and voids (red) (Fig. 3c–f). The volume fraction of voids reduces by 79% after thermal treatment (Table S2, ESI†), which indicates the flowing liquid MOF state is very effective in reducing meso- and macroscale defects.

Zn 2p X-ray photoelectron spectra (XPS) of $ZIF-62-bIm_{0.05}$ exhibit two intense peaks at around 1021 and 1044 eV (Fig. S12, ESI†), which correspond to the $2p_{3/2}$ and $2p_{1/2}$ components respectively. Both peaks slightly shift towards higher binding energy after the vitrification, which could be attributed to the change of Zn oxidation state because of the formation of undercoordinated metal sites after the vitrification. For $(ZIF-62)_{0.2}(6FDA-DAM)_{0.8}$ (Fig. 4), peaks at around 532 and 533 eV in the O 1s spectra are attributed to C=O and C–O groups in 6FDA-DAM.[30] A new fitted peak at 530.6 eV appears in the spectrum of $(a_gZIF-62)_{0.2}(6FDA-DAM)_{0.8}$, which may indicate some Zn–O bonding.[31] In addition, the emerging peak at 684.7 eV in F 1s spectrum after thermal treatment may indicate the formation of Zn–F bonds.[32] Such an observation align with the Zn LMM Auger spectra for composite membrane before and after *in situ* melting (Fig. S14, ESI†). These XPS results indicate that melting of ZIF-62 within the polyimide matrix may occur alongside binding of Zn to both O and F from the 6FDA-DAM matrix.

The formation of new interfacial coordinative bonds can effectively promote the rigidity of polymeric matrix, which was probed by DSC (Fig. S15, ESI†). For the $(a_gZIF-62)_x(6FDA-DAM)_{1-x}$ composite, one major glass transition (T_g) can be identified at *ca.* 390 °C. The T_g of $a_gZIF-62-bIm_{0.05}$, which sits *ca.* 300 °C in its pure phase (Fig. S16, ESI†), is unobservable.[24] The T_g at *ca.* 390 °C is
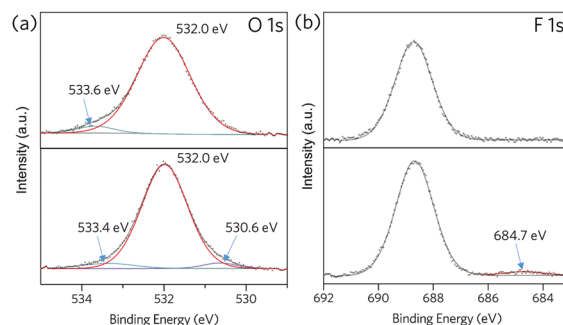

Fig. 4 XPS spectra for $(ZIF-62)_{0.2}(6FDA-DAM)_{0.8}$ (top) and $(a_gZIF-62)_{0.1}(6FDA-DAM)_{0.8}$ (bottom), (a): O 1s, (b): F 1s.

assigned to the polymer matrix, reveals the change of polymeric chain rigidity. Compared with the pure 6FDA-DAM (375.4 °C), the *in situ* melting of ZIF-62 in this case slightly raises the T_g for the substrates: 387.4 °C for $(a_gZIF-62)_{0.1}(6FDA-DAM)_{0.9}$, 393.3 °C for $(a_gZIF-62)_{0.2}(6FDA-DAM)_{0.8}$ and 388.8 °C for $(a_gZIF-62)_{0.3}(6FDA-DAM)_{0.7}$ (Table S3, ESI†). This suggests an enhanced stiffness and restricted motion of the polymer chains.[33]

To further study the change of composite properties after *in situ* ZIF melting, the gas separation performance of the composite was measured with CO_2 and N_2 (Fig. 5 and Table S4, ESI†). The pristine 6FDA-DAM membrane shows a CO_2 permeability of 752.0 Barrer with a CO_2/N_2 selectivity of 17.2. The addition of up to 20 wt% of crystalline $ZIF-62-bIm_{0.05}$ leads to a slightly decreased CO_2 permeability accompanied with a marginal enhancement (*ca.* 10%) in selectivity. This is consistent with the presence of ZIF-62, which occupies the free volume between the 6FDA-DAM chains, reducing the gas diffusion through the membrane. The solubility and the sorption affinity of the membrane for CO_2 can be increased over N_2, as demonstrated by the low adsorption capability of ZIF-62 for N_2 at 303 K (Fig. S6, ESI†). As a result, the $(ZIF-62)_{0.2}(6FDA-DAM)_{0.8}$ displays a greater selectivity compared to the neat polymer membrane. Further increase in filler loading was observed to lead to lower selectivities, ascribed to the formation of interfacial voids.

We then studied the effect of thermal treatment on membrane performance. In the case of $(a_gZIF-62)_x(6FDA-DAM)_{1-x}$, all membranes present decreased CO_2 permeability, with a significantly enhanced selectivity. For example, despite a lowering in CO_2 permeability of *ca.* 22%, the $(a_gZIF-62)_{0.2}(6FDA-DAM)_{0.8}$ displays a 57% increase in CO_2/N_2 selectivity with compared to the pure polymer membrane after the thermal treatment. Compared with $(ZIF-62)_{0.2}(6FDA-DAM)_{0.8}$, $(a_gZIF-62)_{0.2}(6FDA-DAM)_{0.8}$ exhibits a 23.7% increase in CO_2/N_2 selectivity with only a 13.5% decrease in CO_2 permeability. The melting of ZIF-62 significantly enhances the interfacial interaction between $a_gZIF-62-bIm_{0.05}$ and polymer matrices, which reduces nonselective interfacial voids and rigidifies the polymer chains. Furthermore, $a_gZIF-62-bIm_{0.05}$ exhibits extremely low uptake of N_2 and very high CO_2/N_2 sorption selectivity at membrane operation temperature (303 K), the presence of $a_gZIF-62-bIm_{0.05}$ enhances the difference of solubility and sorption affinity for CO_2 over N_2, benefiting the higher selectivity of membranes.

In summary, the application of glassy MOFs are only starting to be explored, and this study demonstrates the proof of
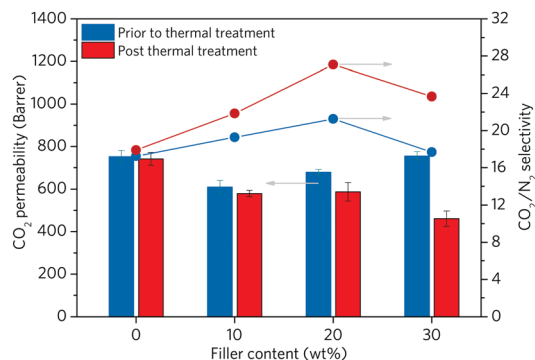
Fig. 5 Gas separation performance of the pure and composite membranes containing up to 30 wt% of MOF fillers. Both membranes before thermal treatment (blue) and after thermal treatment (red) are presented.

concept of *in situ* fabrication of glassy MOF/polymer composite. ZIF-62 crystals have been shown to undergo melting within polymeric matrices. The array of experimental characterisations shows the *in situ* melting within matrics effectively heals the defects even at meso- and macroscale. The dynamically under-coordinated metal nodes and organic ligands in the liquid phase conformation form bonds with polymeric matrices, rigidifying the polymer chains. These findings are encapsulated by membrane molecular separation performances, revealing that the *in situ* melting effectively promotes the membrane selectivity. This results presented here, together with recent progress on fabricating hybrid glass MOF and composite glass MOFs,[34,35] may provide further insights into the huge potential of glassy MOF based composites, such as solid electrolytes, ion conduction, and catalysis.

Conflicts of interest

There are no conflicts to declare.

Notes and references

1 J. Yu, C. Mu, B. Yan, X. Qin, C. Shen, H. Xue and H. Pang, *Mater. Horiz.*, 2017, **4**, 557–569.
2 M.-X. Wu and Y.-W. Yang, *Adv. Mater.*, 2017, **29**, 1606134.
3 H. Kim, S. Yang, S. R. Rao, S. Narayanan, E. A. Kapustin, H. Furukawa, A. S. Umans, O. M. Yaghi and E. N. Wang, *Science*, 2017, **356**, 430–434.
4 T. Tian, Z. Zeng, D. Vulpe, M. E. Casco, G. Divitini, P. A. Midgley, J. Silvestre-Albero, J.-C. Tan, P. Z. Moghadam and D. Fairen-Jimenez, *Nat. Mater.*, 2018, **17**, 174–179.
5 J. Hou, A. F. Sapnik and T. D. Bennett, *Chem. Sci.*, 2020, **11**, 310–323.
6 Q. L. Zhu and Q. Xu, *Chem. Soc. Rev.*, 2014, **43**, 5468–5512.
7 R. Lin, B. Hernandez, L. Ge and Z. Zhu, *J. Mater. Chem. A*, 2018, **6**, 293–312.
8 M. S. Denny, J. C. Moreton, L. Benz and S. M. Cohen, *Nat. Rev. Mater.*, 2016, **1**, 16078.
9 H. Zhu, L. Wang, X. Jie, D. Liu and Y. Cao, *ACS Appl. Mater. Interfaces*, 2016, **8**, 22696–22704.
10 A. M. Marti, S. R. Venna, E. A. Roth, J. T. Culp and D. P. Hopkinson, *ACS Appl. Mater. Interfaces*, 2018, **10**, 24784–24790.
11 R. Lin, L. Ge, L. Hou, E. Strounina, V. Rudolph and Z. Zhu, *ACS Appl. Mater. Interfaces*, 2014, **6**, 5609–5618.
12 L. Ge, W. Zhou, V. Rudolph and Z. H. Zhu, *J. Mater. Chem. A*, 2013, **1**, 6350–6358.
13 W. Liang, L. Li, J. Hou, N. D. Shepherd, T. D. Bennett, D. M. D'Alessandro and V. Chen, *Chem. Sci.*, 2018, **9**, 3508–3516.
14 R. Lin, L. Ge, S. Liu, V. Rudolph and Z. Zhu, *ACS Appl. Mater. Interfaces*, 2015, 7, 14750–14757.
15 R. Lin, L. Ge, H. Diao, V. Rudolph and Z. Zhu, *ACS Appl. Mater. Interfaces*, 2016, **8**, 32041–32049.
16 M.-T. Vu, R. Lin, H. Diao, Z. Zhu, S. K. Bhatia and S. Smart, *J. Membr. Sci.*, 2019, **587**, 117157.
17 A. Kertik, L. H. Wee, M. Pfannmöller, S. Bals, J. A. Martens and I. F. J. Vankelecom, *Energy Environ. Sci.*, 2017, **10**, 2342–2351.
18 T. D. Bennett and S. Horike, *Nat. Rev. Mater.*, 2018, **3**, 431–440.
19 Y. Wang, H. Jin, Q. Ma, K. Mo, H. Mao, A. Feldhoff, X. Cao, Y. Li, F. Pan and Z. Jiang, *Angew. Chem., Int. Ed.*, 2020, **59**, 4365–4369.
20 R. Gaillac, P. Pullumbi, K. A. Beyer, K. W. Chapman, D. A. Keen, T. D. Bennett and F.-X. Coudert, *Nat. Mater.*, 2017, **16**, 1149–1154.
21 J. Hou, C. W. Ashling, S. M. Collins, A. Krajnc, C. Zhou, L. Longley, D. N. Johnstone, P. A. Chater, S. Li, M.-V. Coulet, P. L. Llewellyn, F.-X. Coudert, D. A. Keen, P. A. Midgley, G. Mali, V. Chen and T. D. Bennett, *Nat. Commun.*, 2019, **10**, 2580.
22 J. Hou, M. L. Rios Gomez, A. Krajnc, A. McCaul, S. Li, A. M. Bumstead, A. F. Sapnik, Z. Deng, R. Lin, P. A. Chater, D. S. Keeble, D. A. Keen, D. Appadoo, B. Chan, V. Chen, G. Mali and T. D. Bennett, *J. Am. Chem. Soc.*, 2020, **142**, 3880–3890.
23 S. Li, R. Limbach, L. Longley, A. A. Shirzadi, J. C. Walmsley, D. N. Johnstone, P. A. Midgley, L. Wondraczek and T. D. Bennett, *J. Am. Chem. Soc.*, 2019, **141**, 1027–1034.
24 L. Frentzel-Beyme, M. Kloss, P. Kolodzeiski, R. Pallach and S. Henke, *J. Am. Chem. Soc.*, 2019, **141**, 12362–12371.
25 C. Zhou, L. Longley, A. Krajnc, G. J. Smales, A. Qiao, I. Erucar, C. M. Doherty, A. W. Thornton, A. J. Hill, C. W. Ashling, O. T. Qazvini, S. J. Lee, P. A. Chater, N. J. Terrill, A. J. Smith, Y. Yue, G. Mali, D. A. Keen, S. G. Telfer and T. D. Bennett, *Nat. Commun.*, 2018, **9**, 5042.
26 L. Hamon, N. Heymans, P. L. Llewellyn, V. Guillerm, A. Ghoufi, S. Vaesen, G. Maurin, C. Serre, G. De Weireld and G. D. Pirngruber, *Dalton Trans.*, 2012, **41**, 4052–4059.
27 M. Safak Boroglu and A. B. Yumru, *Sep. Purif. Technol.*, 2017, **173**, 269–279.
28 L. Ge, R. Lin, L. Wang, T. E. Rufford, B. Villacorta, S. Liu, L. X. Liu and Z. Zhu, *Sep. Purif. Technol.*, 2017, **173**, 63–71.
29 R. Lin, L. Ge, H. Diao, V. Rudolph and Z. Zhu, *J. Mater. Chem. A*, 2016, **4**, 6084–6090.
30 G. P. López, D. G. Castner and B. D. Ratner, *Surf. Interface Anal.*, 1991, **17**, 267–272.
31 L.-J. Meng, C. P. Moreira de Sá and M. P. dos Santos, *Appl. Surf. Sci.*, 1994, **78**, 57–61.
32 H. Y. Xu, Y. C. Liu, J. G. Ma, Y. M. Luo, Y. M. Lu, D. Z. Shen, J. Y. Zhang, X. W. Fan and R. Mu, *J. Phys.: Condens. Matter*, 2004, **16**, 5143–5150.
33 M. Valero, B. Zornoza, C. Téllez and J. Coronas, *Microporous Mesoporous Mater.*, 2014, **192**, 23–28.
34 C. W. Ashling, D. N. Johnstone, R. N. Widmer, J. Hou, S. M. Collins, A. F. Sapnik, A. M. Bumstead, P. A. Midgley, P. A. Chater, D. A. Keen and T. D. Bennett, *J. Am. Chem. Soc.*, 2019, **141**, 15641–15648.
35 L. Longley, S. M. Collins, C. Zhou, G. J. Smales, S. E. Norman, N. J. Brownbill, C. W. Ashling, P. A. Chater, R. Tovey, C.-B. Schönlieb, T. F. Headen, N. J. Terrill, Y. Yue, A. J. Smith, F. Blanc, D. A. Keen, P. A. Midgley and T. D. Bennett, *Nat. Commun.*, 2018, **9**, 2135.